Chalcogenide Letters Vol. 19, No. 4, April 2022, p. 267 - 276

Yb/WO_3/Ga_2S_3/Au multifunctional electronic hybrid devices fabricated as tunneling diodes, MOSFETS, microwave resonators and 5G band pass/reject filters

A. F. Qasrawi[a,b,*], S. N. Abu Alrub[a]
[a]*Department of Physics, Arab American University, Jenin, Palestine*
[b]*Department of Electrical and Electronics Engineering, Istinye University, 34010, Istanbul, Turkey*

Herein, Tungsten trioxide-gallium sulfide heterojunctions which are prepared by the thermal evaporation technique under a vacuum pressure of 10^{-5} mbar are employed as active media to fabricate a multifunctional device. The WO_3/Ga_2S_3 (WG) heterojunctions which are deposited onto Yb substrates and top contacted with Au pads of areas of 1.5×10^{-2} cm^2 displayed electronic hybrid device structure composed of two Schottky arms connected to a *pn* junction. The constructed Yb/WG/Au devices showed tunneling diode characteristics with current conduction dominated by thermionic emission and quantum mechanical tunneling. In additions, the capacitance-voltage characteristic curves indicated the formation of PMOS and NMOS under reverse and forwards biasing conditions demonstrating a metal oxide semiconductor fields effect (MOSFET) transistor characteristics. Moreover, the impedance spectroscopy tests on the devices have shown that the device can perform as tunable microwave resonator suitable for 5G technologies. The resonator showed frequency based capacitance tunability and displayed microwave band pass/reject filter characteristics. The microwave cutoff frequency of the Yb/WG/Au band filters reaches 9.65 GHz with voltage standing wave ratios of 1.06 and return loss factor of ~29 dB.

(Received November 28, 2021; Accepted April 11, 2022)

Keywords: WO_3/Ga_2S_3 MOSFETs, Tunneling diodes, Microwave resonators, 5G technology

1. Introduction

Recently, a significant focus is given for the fabrication of band pass/reject filters that suits 5G technologies. As for examples, graphene assembled films (GAF) are employed for the fabrication of compact 5G dual-wideband bandpass filter (DBPF) [1]. The GAF films is mentioned satisfying the requirements of the sub-6 GHz bands. The filters displayed high integration and high information transmission rate for 5G wireless communication [1]. These DBPF exhibited two passbands centered at frequencies of 2.14 and 3.5 GHz. The attenuation level for these band filters exceeds 20 dB at 7.52 GHz [1]. In addition, efficient band-stop filters with cutoff frequency larger than 0.69 GHz are fabricated by the microstrip technology [2]. The rejection levels of these filters are ~35 dB in a rejection bandwidth of 0.25 GHz. Alternatively, ceramics technology is also used to fabricate compact size of 5G band filters. A dielectric filter that suits 5G band showed a pass-band of 3.4 ~ 3.5 GHz [3]. The return loss, insertion loss and voltage standing wave ratios (VSWR) for this dielectric resonator are larger than 15 dB, less than 0.35dB, and 1.62, respectively [3].

On the other hand, metal oxide semiconductor field effect transistors (MOSFET) technology which can also be used as band filters in 5G technologies is used to reduce the effect of the interference caused by signal reflections from circulators in 5G base stations [4]. Literature data suggested that the CMOS technology is one of the best solutions arising with the scaling issues in the world of 5G technology [5]. One of the oxides that is nominated as material suitable for MOSFET fabrication is WO_3 [6-9]. A p-type Diamond: H/WO_3 MOSFET based on surface transfer doping is mentioned showing excellent output characteristics, gate-controllable 2-D hole gas and low gate leakage currents [6]. Thus, here in this work, we are motivated to use WO_3 as p −type oxide layers to fabricate MOSFET device operative as 5G band filters. The epilayer of the

* Corresponding author: atef.qasrawi@aaup.edu

MOSFET is to be made of $n-$type Ga_2S_3. Ga_2S_3 is selected because of its suitability for gigahertz terahertz applications [10, 11]. They are mentioned forming tunneling barriers which can be employed as microwave resonators. The basic characteristics of the currently reported WO_3/Ga_2S_3 heterojunction devices are explored by the X-ray diffraction and energy dispersive X-ray diffraction techniques. The tunneling barrier property of the device is determined via current-voltage and capacitance-voltage characteristics curves. The application as microwave resonator and as band pass/reject filter is tested via impedance spectroscopy technique. The latter test include the conductivity, capacitance, impedance, magnitude of reflection coefficient and return loss spectra in the frequency domain of 0.01-1.80 GHz.

2. Experimental details

Tungsten trioxide and gallium sulfide thin films are deposited onto clean Ytterbium substrates. The heterojunction layers are coated in NORM VCM-600 thermal evaporator under a vacuum pressure of 10^{-5} mbar. The materials used for growing the layers are WO_3 powders (0.20 g, Alpha Aeser, 99.8%), Ga_2S_3 powders (0.2 g, Alpha Aeser,99.99%) and ytterbium crystal lumps (99.99%). The substrate holder was located 15 cm above the evaporation heater. The growth cycles is initiated by growing WO_3 films of thicknesses of 1.0μm. The freshly resulting WO_3 films were recoated with Ga_2S_3 films of thicknesses of 1.0 μm. For the purpose of Au contact pads coating, the produced $Yb/WO_3/Ga_2S_3$ is masked with rectangular masks of areas of 1.5×10^{-2} cm^2. In each cycle, 10 slides of 2.5×7.5 cm^2 are produced. On each slide more than sixty Au pads devices can be produced. The thickness of the films was measured with the help of an in situ Inficon STM-2 thickness monitor installed in the evaporator. The structure of the films is explored via Minflex 600 diffractometer. The current (I)-voltage (V) characteristics is recorded using Keithley $I-V$ system equipped with Keithley 6485 Picoammeter, Keithley 230 programmable voltage source and sample fixture. The system is controlled via MATLAB software packages. The impedance spectra are measured using Agilent 4291B 0.01-1.80 GHz impedance analyzer. The conductivity type of the films as $p-$ WO_3 and $n-$ Ga_2S_3 type was determined by the hot probe technique.

3. Results and discussion

3.1. Design considerations

In this work, we consider the design and characterization of $Yb/WO_3/Ga_2S_3/Au$ (Yb/WG/Au) electronic hybrid devices. In accordance with the energy band diagram which is illustrated in Fig. 1, the electron affinity, energy band gap and work function of $p-WO_3$ are $q\chi_1$ =3.33 eV, $E_{g1}=3.21$ eV (experimentally determined in our laboratory) and $q\phi_1$ =4.80-5.30 eV [7-8] (average value is 5.05 eV [9]), respectively. Those of $n-Ga_2S_3$ are $q\chi_2=3.30$ eV [10], $E_{g2}=2.60$ eV (experimentally determined in our laboratory) and $q\phi_2$ =3.46 eV [11], respectively. The formation of $p-WO_3/n-Ga_2S_3$ heterojunctions is associated with a conduction and valence band offsets of $\Delta E_c=|q\chi_2-q\chi_1|=0.03$ eV and $\Delta E_v=\Delta E_g-|q\chi_2-q\chi_1|=0.58$ eV, respectively [12]. The built in potential across the pn junction is $qV_{bi-pn}=|q\phi_1-q\phi_2|=$ 1.59 eV [12]. However, since the metal work function of Yb being 2.51 eV [13] is less than that of $p-WO_3$, $Yb/p-WO_3$ form a Schottky arm of barrier height of $q\phi_{b1}=\left|E_{g1}-q\phi_{Yb}+q\chi_1\right|=$ 4.03 eV. The built in potential at this interface is $qV_{bi1}=|q\phi_{Yb}-q\phi_1|=2.54$ eV Similarly, at the $Au/n-Ga_2S_3$ interface, the gold work function being 5.34 eV [13] is larger than that of Ga_2S_3 (3.46 eV) leading to a barrier height of $q\phi_{b2}=|q\phi_{Au}-q\chi_1|=2.04$ eV. The built in potential at the Au/n-Ga_2S_3 is $qv_{bi2}=|q\phi_{Au}-q\phi_2|=1.88$ eV. Hence electrical conduction in the device is resisted by three barriers and the biasing potential need to overcome the three built in potentials. Hybrid electronic devices gain importance because of their ability to handle more than one duty at a time [14, 15].

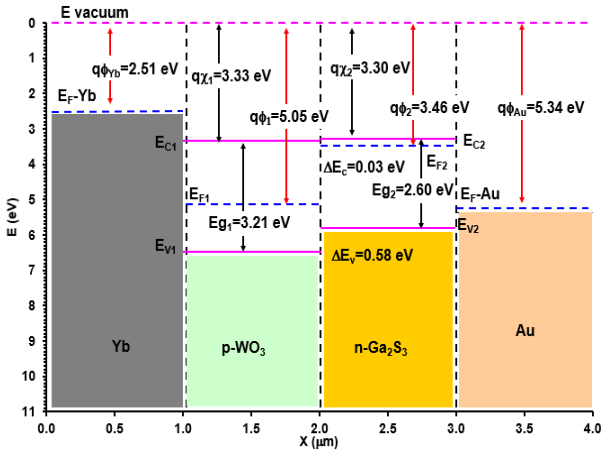

Fig. 1. The energy band diagram for the Yb/WO_3/Ga_2S_3/Au heterojunctions.

3.2. Structural and compositional analyses

The optical image for the experimentally designed Yb/WO_3/Ga_2S_3/Au hybrid electronic devices is shown in the inset of Fig. 2. The total area (A) of the device is ~1.5×10^{-2} cm^2. Fig. 2 also display the X-ray diffraction (XRD) patterns for the grown layers. In general, the crystal structure of the samples is amorphous. Some weak reflections appeared in the XRD patterns. Analysis of the observed patterns which were carried out using "Crystydiff" software packages allowed prediction of the possible structures. Since the number of observed XRD peaks is insufficient to compute the basic properties of the crystal structure, assignment of the observed peaks was based on powder diffraction files (PDF). The XRD of the PDF of orthorhombic WO_3 is plotted by black colored lines in Fig. 2. The consistency of the observed peaks with the theoretical estimation gives evidence about the formation of orthorhombic WO_3 (PDF card no: 32-1395) [16] in addition to the cubic Yb (PDF card no: 00-002-1367). Probable formation of monoclinic Ga_2S_3 can also be guessed from the peak which is detected at diffraction angles of $2\theta = 25.70^o$ (PDF card no: 00-016-0500). On the other hand, the compositional analyses which were carried out by the energy dispersive X-ray spectroscopy (EDS) technique indicated that the stacked layers of WO_3/Ga_2S_3 are composed of 37.74 at. % Ga and 62.26 at. % S revealing the formation of $Ga_2S_{3.30}$ and 22-25.0% W and 70-75.0 at. % oxygen resulting in the stoichiometric formation of WO_{3-x}. However, from growth cycle to cycle and from one sample to another of similar or different growth cycles, the oxygen content vary by ~$\mp$0.2.

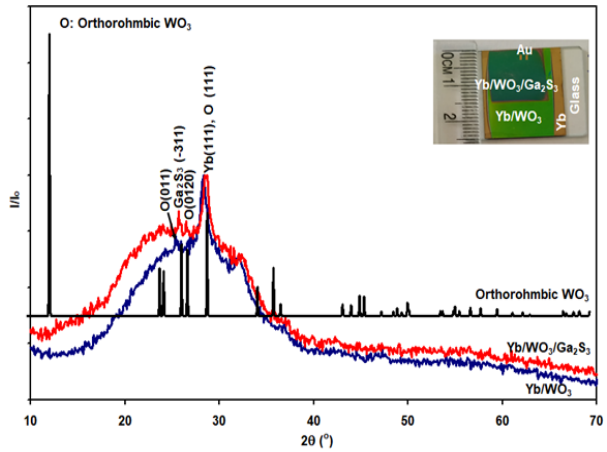

Fig. 2. The X-ray diffraction patterns for the Yb/WO_3 and Yb/WO_3/Ga_2S_3 heterojunctions. The inset show the optical image of the fabricated device.

3.3. Current-voltage characteristics

The current (I)-voltage (V) characteristics curves for the Yb/WG/Au hybrid devices is shown in Fig. 3 (a). The curve represents rectifying diode characteristics. It is also evident from the curve that a large leakage current is generated under reverse biasing conditions. Large leakage currents in hybrid electronic devices originate from the leakage of minority carriers across the pn junction. If it results from the Schottky arm, then, it is due to thermionic emission of electrons from metal to a semiconductor [12, 17]. In our hybrid device, the forward current is supplied from the Yb/WO_3 side setting this Schottky arm and the pn junction is forward biased. Since holes are pushed forward and the negative terminal is connected to Au side, then, Au/Ga_2S_3 Schottky barrier is reverse biased. On the other hand, when positive terminals are connected to Au/Ga_2S_3 side, the other parts of the device are reverse-biased. Thus, there is always a chance for charge carriers to flow from metal to semiconductors forcing the flowing of an extra tunneling current in the reversing direction. Tunneling currents also accounts for the large leakage current values [12, 18]. In addition, a charge carrier recombination in depletion regions through trap levels presumably associated with crystal defects could also be a reason for the observed large leakage current values [18]. The grown layers are mostly amorphous (XRD analyses) indicating the presence of large number of defects in the samples.

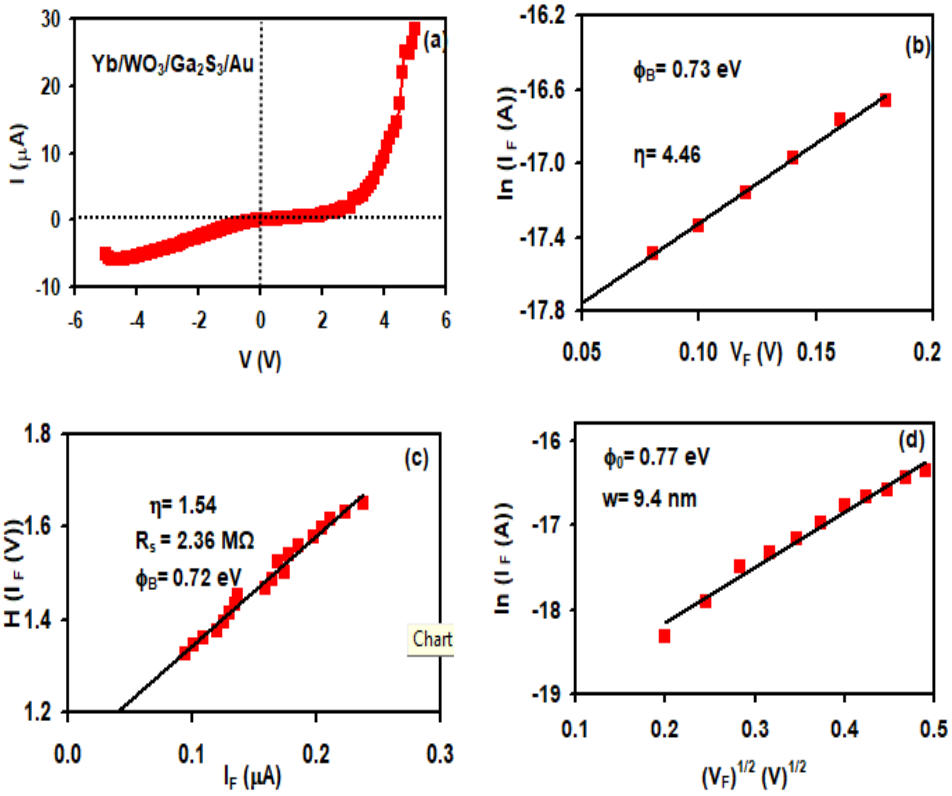

Fig. 3. (a) The current-voltage characteristics, (b) The $ln(I) - V$ variations showing the conduction by thermionic emission, (c) the Cheung's functional analyses and (d) the $ln(I) - \sqrt{V}$ variation showing the tunneling process in the Yb/WO_3/Ga_2S_3/Au devices.

The current-voltage characteristic curves are analyzed in accordance with the Schottky thermionic emission theory which state that current flows in the device through thermionic emission of charge carriers over the Schottky barrier heights ($q\phi_b$). In this case,

$$I = AA^*T^2 e^{q\phi_b/kT}\left(e^{qV/\eta kT} - 1\right). \quad (1)$$

Here, $A^* = 120m^*_{WG}$ is Richardson constant calculated from the rule $m^*_{WG} = \left(m^{*-1}_{WO3} + m^{*-1}_{Ga2S3}\right)^{-1}$ representing the reduced effective mass of the WG system. The hole effective mass for WO_3(m^*_{WO3}) is 0.94 m_o [36] and electron effective mass (m^*_{Ga2S3}) for Ga_2S_3 is 0.40 m_o[11]. Substituting the reduced effective mass as $0.28m_o$ one reveals A^* value of 33.6 A/(cm^2K^2). As illustrated in Fig. 3 (b), the linear plots of the $\ln(I) - V$ variations in accordance with Eqn. (1) reveal an ideality factor (η) of 4.46 and 4.96 and barrier heights of 0.73 eV and 0.72 eV under forward and reverse biasing conditions, respectively. Considering the diode series resistance (R_s) as one main reason for the deviation of the ideality factor from linearity, the Cheung's function ($H(I)$) for $I - V$ analyses are executed. In accordance with this model the current takes the form [21],

$$I = AA^*T^2e^{q\phi_b/kT}\left(e^{(qV - IR_{S)}/\eta kT} - 1\right). \quad (2)$$

The series resistance, barrier height and ideality factors are determined from the relations,

$$\frac{dV}{dln(I)} = IR_s + n(\frac{kT}{q}) \quad (3)$$

$$H(I) = V - \eta\left(\frac{kY}{q}\right)\ln(\frac{I}{AA^*T^2}) = IR_s + \eta q\phi_b \quad (4)$$

The slope and intercept of the linear fit of the $H(I) - I$ variations which is shown in Fig. 3 (c) resulted in η, R_s and $q\phi_b$ values of 1.54 and 1.0, 2.82 MΩ and 1.08 MΩ and 0.72 and 0.51 eV, under forward and reverse biasing conditions, respectively. Even though the series resistance effect is reduced, the ideality factor deviates from unity under forward biasing conditions. $\eta = 1.0$ values indicate domination of diffusion currents while $\eta = 2.0$ values means the recombination current dominates [12]. When both of the diffusions and recombination currents are dominant $1.0 < \eta < 2.0$. Hence, the dominant current conduction is governed by both mechanisms. On the other hand, considering the existence of the quantum mechanical tunneling mechanisms as a reason for current conduction across the barriers, then the current in the devices follows the relations [22],

$$I = AA^{**}T^2V^{\gamma}\exp(-\frac{e\Phi}{kT}) \quad (5)$$

$$\Phi = \phi_o - n\sqrt{e\eta/(4\pi\varepsilon_o\varepsilon_r)}\,\sqrt{V}/\sqrt{w}\,. \quad (6)$$

Here, Φ is the electric field-dependent activation energy that represents a Schottky-barrier height in the presence of the electric field, $q\phi_o \equiv q\phi_b$ is the field independent value. For Schottky-Richardson field emission (tunneling) mechanism to dominate, the ideality factor $n = \eta =$ 1.0 and $\gamma = 0$ are substituted. The linear plots of the $\ln(I) - \sqrt{V}$ variations which are presented in Fig. 3 (d), indicate the dominations of the field assisted tunneling current through barrier of heights and widths (W) of 0.77 eV and 0.77 eV and 9.4 nm and 6.8 nm, under forward and reverse biasing conditions, respectively. The barrier height values obtained assuming thermionic and electric field assisted thermionic emission (tunneling) under forward biasing conditions are comparable to each other assuring the possible domination of both mechanisms. However, under reverse biasing condition, the lower barrier height ($q\phi_b = 0.51$ eV) in which the thermionic emission dominates and the very narrow barrier width (6.8 nm) in which the charge carriers tunnel through is a clear reason for the existence of large leakage current in the hybrid devices.

3.4. MOSFET characteristics

The capacitance (C)-voltage (V) characteristics curves for the Yb/WG/Au devices is shown in Fig. 4 (a). The impeded ac signal was of amplitude of ~0.10 V and the signal frequency was 1.0 MHz. . In accordance with Fig. 4 (a), the $C - V$ curve show the formation of an inverted PMOS (metal oxide semiconductor) channels when device is reverse biased and inverted NMOS channel characteristics when the Yb/WG/Au hybrid electronic devices are forward biased

[12, 22]. It is evident from the figure that, both of the NMOS and PMOS channels display depletion, inversion and accumulation modes of operation. Namely, for NMOS channel (Yb/WO_3), applying small positive voltage drives away the valance band edge from the Fermi level. At the same moment, holes are also driven away from the gate resulting in low carrier density. As a result, the capacitance displays the valley that appears in the voltage range of -0.70-0.66 V. Increasing the voltage at the gate furthers, brings the conduction band edge closer to the Fermi level. Such behavior increases the number of surface electrons allowing the formation of the inversion layer or (N-channel) at the WO_3 side [12, 22]. In order to obtain information about the MOSFET operation parameters (qV_{bi}, N':free carrier density) in the PMOS and NMOS channels, the depletion region of $C-V$ characteristic curve is analyzed using the equation [12, 22],

$$C^{-2} = \frac{2(V_{bi} - V - \frac{2kT}{q})}{q\varepsilon_r N'}. \tag{7}$$

The slope and intercepts of the linear plots of the $C^{-2}-V$ variations which are illustrated in Fig. 4 (b) reveal $qV_{bi-PMOS} = 2.49$ eV, $qV_{bi-NMOS} = 1.93$ eV. The values are comparable with the (not inverted) theoretically estimated flat band built in potential values as 2.54 eV and 1.88 eV at the Yb/p-WO_3 and Au/n-Ga_2S_3 sides, respectively. The calculated values of the N'_{PMOS} and N'_{NMOS} is 1.40×10^{19} cm^{-3} and 7.61×10^{18} cm^{-3}, respectively. In addition, substituting the effective dielectric constant $\varepsilon_r = (\varepsilon_{r-WO3}^{-1} + \varepsilon_{r-Ga2S3}^{-1})^{-1} = (3.6^{-1} + 3.5^{-1})^{-1}$ [20] as 1.77, the depletion widths ($W_{N,P} = \sqrt{2\varepsilon_r(V_{bi})/(qN')}$) [12] of the PMOS and NMOS channels are determined and found to exhibit values of 5.90 nm and 7.00 nm, respectively. The values of the inverted channel widths are comparable with those we obtained from the analysis of the current-voltage characteristics.

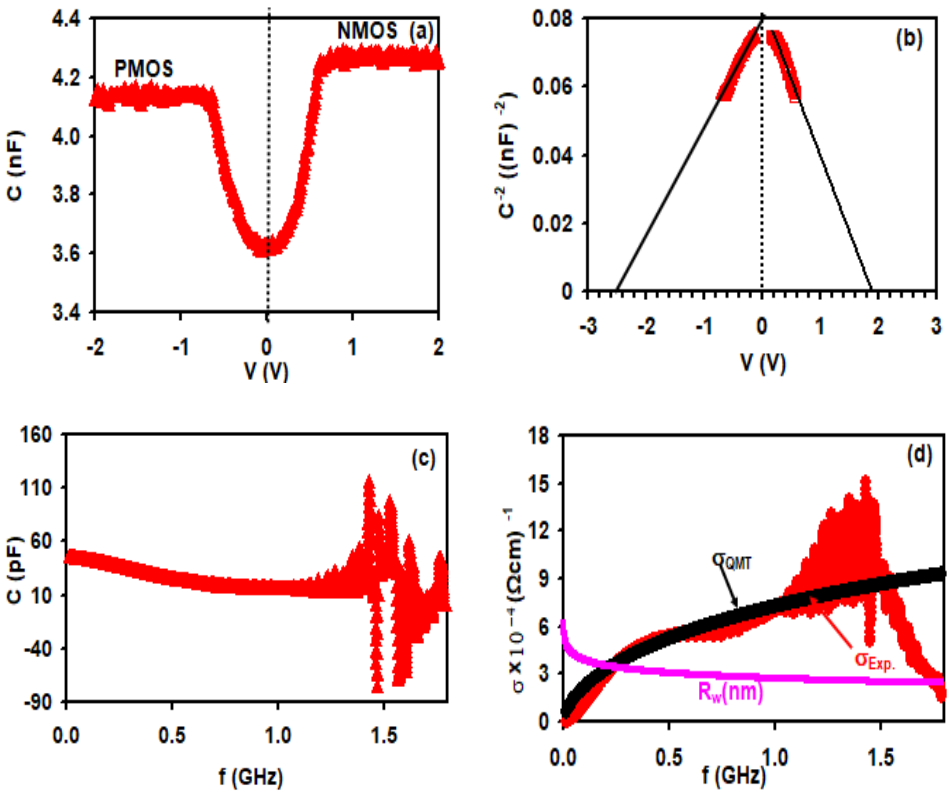

Fig. 4. (a) the capacitance-voltage characteristics, (b) the $C^{-2}-V$ variations in the depletion region, (c) the capacitance spectra and (d) the conductivity and tunneling distance spectra for the Yb/WO_3/Ga_2S_3/Au as MOSFET devices.

3.5. Microwave resonator characteristics

In order to observe further facilities of the Yb/WG/Au electronic hybrid devices, the capacitance and conductivity spectra of the devices were recorded in the spectral range of 0.01-1.80 GHz. The respective spectra are Illustrated in Fig. 4 (c) and (d). The capacitance spectra display a decreasing trend of variation in the spectral range of 0.01-1.45 GHz. In the range of 1.45 -1.80 GHz, the capacitance spectra display set of sequential resonance-antiresonance peaks. The most pronounced peak is centered at 1.47 GHz. When the capacitance is in the antiresonance mode, the capacitance value is negative. Resonance-antiresonance phenomenon which is associated with negative capacitance effect is observed near 1.26 GHz in (Al, Yb)/Ga_2S_3/Au [11]. It is also observed in Al/Ge/In_2Se_3/Ga_2S_3/Al hybrid structures at 0.18 GHz [10]. This physical phenomenon is important as it indicates the applicability of the Yb/WG/Au devices as negative capacitance source at high frequencies. It is useful for noise reduction and signal amplification. Negative capacitance effect can be attributed to non-radiative recombination of injected carriers into trap levels associated with defects, or due to the capture-emission of injected carriers between multilevels [23].

Fig. 4 (d) illustrate the conductivity spectra for the Yb/WG/Au devices. It is clear from the figure that the conductivity increases with increasing signal frequency in the frequency domain of 0.1-0.35 GHz. In the spectral range of 0.35-1.10 GHz, the conductivity tends to remain constant following very slow increasing trends of variation. It then increases with increasing frequency displaying a maxima at ~1.43 GHz. In the frequency domain of 1.45-1.80 GHz, the conductivity decreases with increasing frequency. Since the ac conductivity is given by the relation $\sigma = Aw^s$ (A is constant determines the strength of polarization, $w = 2\pi f$), then, $s = dln(\sigma)/dln(w)$ [10]. s is the Jonscher coefficient representing the amount of interactions between the mobile ions and the lattice around them [10, 24, 25, 26]. In accordance with the quantum mechanical tunneling (QMT) model, tunneling of charge carriers between two localized states near the Fermi level dominates when s parameters appreciably decreases with increasing frequency at particular temperature as illustrated in Fig. 5 (a). The conduction by quantum mechanical tunneling is given by the relations [10, 24-26],

$$\sigma_{Tun}(w) = \frac{\pi^4}{24} e^2 kT\alpha^{-1}(N(E_F))^2 w R_w^4 \tag{8}$$

$$R_w = \ln(1/(w\tau_0))/(2\alpha) \tag{9}$$

In the above equations, $N(E_F)$ is the density of localized states near the Fermi level and R_w is the average distance at a particular frequency (w). The theoretically produced ac conductivity is shown by black colored circles in Fig. 4 (d). The theoretical data is reproduced assuming $N(E_F) = 9.1 \times 10^{18}$ (cm^{-3}/eV) and relaxation time constant (τ_o) of 0.70 ps. This value corresponds to the phonon frequency value being 47.62 cm^{-1}. This value is one of the low frequency modes in Ga_2S_3 [27]. The value of α (α^{-1}=10 Å) represents the spatial decay parameter for the wave function employed to represent the localized states. As also shown in Fig. 4 (d), the distance over which the charge carrier hop or tunnel is in the range of 6.20 -2.40 nm. The higher the propagating signal frequency is, the shorter the distance is. The slowest signal corresponds to a tunneling barrier of width of 6.20 nm consistent with the dc analysis carried out in section 3.3 and section 3.4.

3.6. Band filters characteristics

The impedance (Z) spectra which are shown in Fig. 5 (b) exhibit a sharp decrease in the value of Z by two orders of magnitude in a short range of frequency (0.01-0.15 GHz). It then follows slower decreasing trends of variation in the rage of 0.15-1.45 GHz. In the range of 1.45-1.80 GHz, Z increases with increasing frequency. The impedance spectra provide information about the magnitude of the reflection (rejection) coefficient ($\rho = \frac{(Z_{Device} - Z_{source})}{Z_{device} + Z_{source}}$) in the Yb/WG/Au devices. The magnitude of the reflection coefficient spectra is presented in Fig. 5 (c). The figure indicates that ρ tends to exhibit high values for all applied frequencies less than 1.45

GHz. $\rho = 1.0$ means that all incident signals are rejected and $\rho = 0.0$ means all propagating signals are passed. Thus, the Yb/WG/Au devices can be regarded as band reject filters in the frequency domain of 0.01-1.45 GHz and as band pass filters in the frequency domain of 1.45-1.77 GHz. Modeling the reflection coefficient spectra assuming that the device represents an RLC circuit using the relation $Z = R + jwL - jwC$ (L is inductance) resulted in the fittings shown by black circles in Fig. 5 (c). The fitting was achieved assuming $R = 50\ \Omega$, L =26 nH and C=0.33 pF. The microwave cutoff frequency of this band filter ($f_{co} = (2\pi RC)^{-1}$) at the maximum transmission point (1.77 GHz) is 9.65 GHz. This value is important as it indicate that the Yb/WG/Au devices are employable as band reject filters suitable for 5G technologies. 5G technologies are mentioned operating at different spectrum bands. These bands are categorized into Low-bands (below 1.0 GHz), Mid-bands between 1-6 GHz and High-bands (mm-wave) above 24 GHz [27]. Generally, the Mid-band is preferred because of the propagation losses which will be more at higher frequencies [27]. The most of the operation bands of these filters are reported to be exhibit low voltage standing wave ratio $VSWR$=$(1 + \rho)/(1 - \rho)$)) down to 3.2 or less and return loss ($L_r = -20\log(\rho)$) value higher than 5.6 dB [28]. For Yb/WG/Au devices, the return loss spectra are displayed in Fig. 5 (d). It shows the good performance of the band filters above 1.45 GHz. The $VSWR$ of this device at 1.45 GHz is 4.0 it reaches value of 1.06 at 1.77 GHz. As a result, it is concluded that the fabricated Yb/WG/Au hybrid electronic devices are smart electronic devices which can be employed as band filters in 5G technologies.

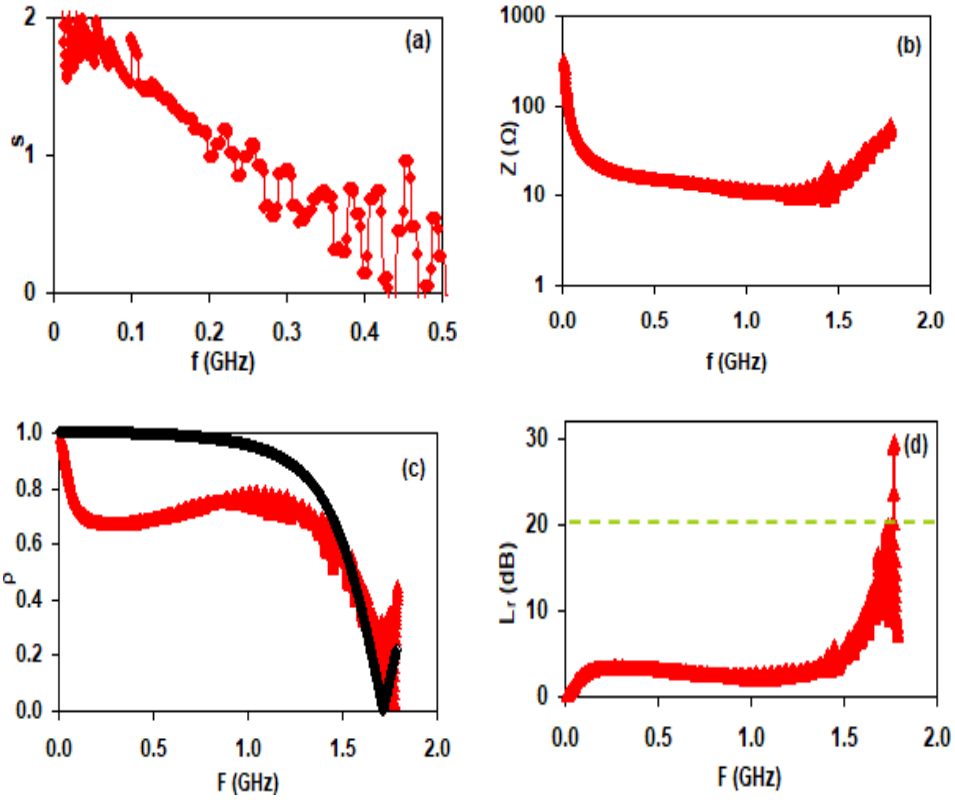

Fig. 5. (a) the exponent s of the $\sigma = Aw^s$ dependence, (b) the impedance spectra, (c) the magnitude of the reflection coefficient spectra and (d) the return loss spectra for the Yb/WO_3/$G_{a2}S_3$/Au as MOSFET band filters.

4. Conclusions

In this article, we have shown the possibility of fabricating new classes of metal oxide semiconductor devices (MOSFET) that can be employed as band pass/reject filters suitable for 5G technologies. The MOSFET device are prepared by depositing WO_3/Ga_2S_3 (WG) onto Yb substrates by the vacuum evaporation technique. The heterojunction devices displayed tunneling diode characteristics and behaved as tunable microwave resonators. The microwave cutoff frequency for these 5G band filters reached 9.65 GHz. The return loss and voltage standing waves ratios of the devices are combatable with the values nominated for the 5G technology. The compact size of the device presented by thickness of $\sim 2.0 - 3.0 \mu$m and device surface area of 1.5×10^{-2} cm^2 make it attractive for use in mobile technologies.

Acknowledgements

This work was supported by the Deanship of Scientific Research (DSR), Arab American University, Jenin, Palestine and by DSR of Istinye University, Istanbul, Turkey. The authors, therefore, gratefully acknowledge the DSR technical and financial support.

References

[1] H. Bangqi, S. Li, R. Song, Zh. Hou, Ch. Liu, D. He, High- conductivity graphene-Assembled, e22602 (2021).
[2] O. Fernández, T. Fernández, Á. Gómez, Electronics **10**, 974 (2021).
[3] B. Luo, Zh.-sh. Zhan, B. Fang, J.-B. Zhang, J. of Phys.: Confer. Ser. **1965**, 012060 (2021).
[4] E. O. Omoru, V. M. Srivastava, J. Commun. **15**, 833 (2020).
[5] P. Jakhar, A. Kumar, M. Das, P. Rajagopalan, In CMOS Analog IC Design for 5G and Beyond, p. 15, Springer, Singapore, 2021.
[6] Z. Yin, M. Tordjman, A. Vardi, R. Kalish, J. A. Alamo, IEEE Electron Dev. Lett. **39**, 540 (2018).
[7] Y. Yuan, J. Huang, G. Li, Intermediate layers in tandem organic solar cells **1**, 65 (2011).
[8] I. S. Oh, G. M. Kim, S. H. Han, S. Y. Oh, Electronic Materials Letters **9**, 375 (2013).
[9] G. Halek, I. D. Baikie, H. Teterycz, P. Halek, P. Suchorska-Woźniak, K. Wiśniewski, Sens. & Actuat. B: Chem. **187**, 379 (2013).
[10] A. F. Qasrawi, O. A. Omareya, Thin Solid Films **660**, 276 (2018).
[11] S. R. Alharbi, A. F. Qasrawi, Current Applied Physics **17**, 835 (2017).
[12] S. M. Sze, Y. Li, K. K. Ng, Physics of semiconductor devices. John wiley & sons, 2021.
[13] H. L. Skriver, N. M. Rosengaard, Phys. Rev. B **46**, 7157 (1992).
[14] A. Rasool, R. Amiruddin, S. Kossar, M. C. S. Kumar, J. Appl. Phys. **128**, 044503 (2020).
[15] Z. Xia, P. Gao, T. Sun, H. Wu, Y. Tan, T. Song, Sh.-T. Lee, B. Sun, ACS applied materials & interfaces **10**, 13767 (2018).
[16] D. Hirai, E. Climent-Pascual, R. J.Cava, Physical Review B **84**, 174519 (2011).
[17] S. Arumugam, M. Perumal, K. P. Anjana, S. V. M. Satyanarayna, S. K. Sinh, Physics of Plasmas **27**, 023512 (2020).
[18] J. Back, High-efficiency violet and blue InGaN microcavity light-emitting diodes. University of California, Santa Barbara, 2021.
[19] R. Lin, J. Wan, Y. Xiong, K. Wu, W.-ch. Cheong, G. Zhou, D. Wang, Q. Peng, Ch.Chen, Y., J. Amer.Chem. Soc. **140**, 9078 (2018).
[20] S. R. Alharbi, A. F. Qasrawi, Thin Films," Plasmonics **12**, 1045 (2017).
[21] M. D. Kaya, B. C. Sertel, N. A. Sonmez, M. Cakmak, S. Ozcelik, J. Mater. Sci.: Mater. Electron. **32**, 20284 (2021).
[22] A. F. Qasrawi, N. M. A. Yaseen, IEEE Transactions on Electron Devices (2021).
[23] S. Sanghyun, High frequency MIS-based III-nitride transistor and integrated bio-sensor Technology, University of Michigan, 2009.

[24] S. Sharma, M. M. Singh, K. D. Mandal, Ceram. Trans. **252**, 95 (2015).
[25] N. M. Khusayfan, A. F. Qasrawi, H. K. Khanfar, Mater. Res. Expr. **5**, 026303 (2018).
[26] A. Ghosh, Physical review B **41**, 1479 (1990).
[27] S. R. Thummaluru, M. Ameen, R. K. Chaudhary, IEEE Trans. Anten.Propag. **67**, 5634 (2019).
[28] M. O. Khalifa, A. M. Yacoub, D. N. Aloi, IEEE Transactions on Antennas and Propagation (2021).